ASTM D5946
ASTM D7334
ASTM D7490
ISO 27448

optical contact angle measurements and drop contour analysis to determine surface energy as well as interfacial and surface tension

force tensiometry, dynamic contact angle measurements, and force of adhesion evaluation

ASTM D1331
ASTM D1417
ISO 1409

ISO/TR 13097

optical turbidity, stability and aging analysis of multi-phase dispersions

zeta potential measurements of fibres, powders, and plate-shaped solids

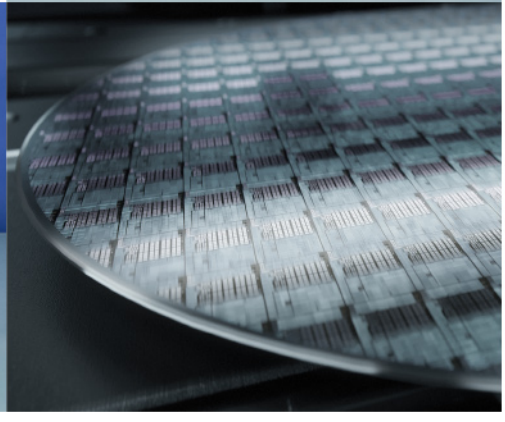

High-end, versatile laboratory measurement device portfolio for a comprehensive analysis of surfaces and interfaces

Learn more >

dataphysics
Understanding Interfaces

DataPhysics Instruments GmbH
Raiffeisenstraße 34 • 70794 Filderstadt, Germany
phone +49 (0)711 770556-0 • fax +49 (0)711 770556-99
sales@dataphysics-instruments.com
www.dataphysics-instruments.com

ADVANCED FUNCTIONAL MATERIALS
www.afm-journal.de

In-Flight Synthesis of Core–Shell Mg/Si–SiO_x Particles with Greatly Reduced Ignition Temperature

Brandon Wagner, Pankaj Ghildiyal, Prithwish Biswas, Mahbub Chowdhury, Michael R. Zachariah, and Lorenzo Mangolini**

Magnesium is a promising candidate as a solid fuel for energetic applications, however, the diffusion-controlled oxidation mechanism impedes its reaction with an oxidizer, often resulting in diminished performance. In this study, non-thermal plasma processing is implemented to modify the surface of magnesium nanoparticles with silicon in-flight, in the gas-phase to enhance the rate of interfacial reactions and tune the ignition pathways. Allowing the silicon coating to partially oxidize provides direct contact between the fuel and oxidizer, resulting in a nanostructured thermite system at the single particle level. The proximal distance between oxidizer and fuel directly impacts the ignition temperature and, therefore, the combustion kinetics. An intermetallic reaction occurs within the magnesium/silicon system to supplement the heating of the magnesium fuel to initiate its reaction with the oxidizer, resulting in highly reduced ignition thresholds. The ignition temperature is lowered significantly from ≈740 °C for magnesium particles with a native oxide layer to ≈520 °C for particles coated via the in-flight plasma process.

1. Introduction

Reducing metal particle size is a common approach toward enhancing the combustion performance of solid fuels, although this approach is not without drawbacks. It results in a significant decrease in active content as size is pushed into the sub-micron regime.[1] Sintering and agglomeration also hinder the complete combustion and energy extraction from solid nanoenergetics.[2] In addition, the reaction kinetics are typically diffusion-limited and are dictated by the properties of the native oxide layer.[3] Among metals, magnesium (Mg) has attracted interest for energetic applications because of its abundance, volatility, and high energy density.[4] The boiling point of Mg is much lower than its oxide (1090 °C < 3600 °C), and as a result, ignition proceeds via outward diffusion of Mg vapor through the native oxide shell.[5] While the porous nature of the oxide layer facilitates the Mg vapor transport, this process remains the rate-limiting step for the ignition of nanoscale Mg particles.[6]

Surface modification has been actively investigated as a means toward the passivation of metal surfaces and the enhancement of interfacial interactions.[7] Guan et al. demonstrated that the combustion of aluminum (Al) particles can be enhanced with the addition of an inorganic coating applied via a heterogeneous nucleation method. The better surface coverage of Al with ammonium perchlorate compared to a mixture of the two allowed for faster decomposition of the oxidizer.[8] Jiang et al. utilized silylation chemistry to apply fluorocarbons to Al nanoparticles (NPs) to improve their reactivity and combustion performance.[9] Jouet et al. used wet-chemistry methods to simultaneously nucleate Al NPs coated with a fluorocarbon coating, to make an oxide free system.[7c] The disadvantage of the coating methods in the aforementioned work is the use of toxic solvents and the required washing and drying steps. Foley et al. discuss the coating of Al NPs with various transition metals to prevent them from oxidizing in air. The active content of Al is higher with a nickel coating compared to the uncoated sample.[10] Ali et al. created core-shell particles composed of an Al core and iron shell by electroless deposition, which exhibited a higher energy release rate than uncoated Al.[11] The approach involved pre-treatment of the powder to remove the alumina layer before applying the metal coating, which introduces a critical step in the synthesis scheme. To our knowledge, there is considerably less work on the coating of Mg powders for combustion applications. One report shows that Mg fuel can be preserved by a paraffin coating using a supercritical solution method.[12] The purpose of the coating is to passivate the Mg surface and stabilize it in air. Hastings et al. successfully coated Mg with siloxane by reactions with cyclic hydridomethylsiloxanes with Mg powder.[13] The coating improves stability compared to uncoated Mg while minimally decreasing the ignition temperature of Mg.

B. Wagner, L. Mangolini
Materials Science and Engineering Program
University of California Riverside
900 University Avenue, Riverside, CA 92521, USA
E-mail: lmangolini@engr.ucr.edu
P. Ghildiyal, P. Biswas, M. Chowdhury, M. R. Zachariah
Department of Chemical and Environmental Engineering
University of California Riverside
900 University Avenue, Riverside, CA 92521, USA
E-mail: mrz@engr.ucr.edu
The ORCID identification number(s) for the author(s) of this article can be found under https://doi.org/10.1002/adfm.202212805.

DOI: 10.1002/adfm.202212805

Motivated by these reports, we explore the gas-phase surface modification of magnesium NPs with the goal of improving their combustion kinetics. In particular, we aim at coating magnesium NPs before they are exposed to air, and we focus on the use of non-thermal plasmas to achieve a high-quality conformal coating on magnesium NPs under anaerobic conditions. Non-thermal plasma processing is a versatile gas-phase synthesis method for nanoparticle production,[14] thin-film deposition,[15] surface modification,[16] and coatings.[17] Non-thermal plasmas offer several advantages over other gas-phase processing methods. The aerosol in a low-temperature plasma becomes negatively charged, preventing agglomeration, and leading to narrower size distributions.[18] The presence of free electrons with temperatures in the range of a few eVs generates highly reactive free-radicals, driving reactions at low gas temperatures. As a result, materials with controllable degree of crystallinity (crystalline or amorphous) can be produced.[19] Moreover, the products have high purity because solvents and ligands are unnecessary. Non-thermal plasmas have been utilized to coat NPs in-flight. For instance, recent work has shown that silicon NPs can be either surface modified with polymer,[20] or coated with carbon.[21] Core–shell semiconducting quantum dots[22] and plasmonic materials[23] have also been generated through in-flight plasma coating.

In this work, we use a non-thermal plasma to coat Mg NPs in-flight with a silicon shell, and we investigate its properties as an energetic material. Thermal evaporation is used to produce an aerosol of Mg NPs starting from a solid Mg source. Ohmic heating of the Mg precursor generates a Mg vapor cloud, while the argon carrier gas quenches the vapor to drive the homogeneous nucleation of NPs.[24] The Mg-laden aerosol is then passed to a non-thermal plasma chamber where the silicon coating is applied in-flight. The addition of a silicon coating serves a dual purpose: it limits the growth of the MgO shell while also achieving direct contact between the fuel (Mg) and an auxiliary oxidizer, since the silicon shell is inevitably partially oxidized. Effectively, this approach leads to the in-flight formation of a nano-thermite, i.e.,—a reactive system in which the metal reducing agent and the oxidizer are placed in close contact. The application of the silicon-based shell directly onto the surface of the Mg NPs leads to short diffusion distances, resulting in a significant reduction in ignition temperature and rapid combustion kinetics for boosted performance when the coated material is ignited with a primary oxidizer such as bismuth oxide (Bi_2O_3).

2. Experimental Section

2.1. In-Flight Coating of Mg Nanoparticles

The experimental setup is shown in **Figure 1** with more details of the setup outlined in the (Figure S1, Supporting Information). Mg NPs were prepared by thermal evaporation, where bulk Mg precursor (≈250 mg) was heated while flowing argon gas at a flow rate of 350 sccm, and the chamber pressure was 40 torr. The Mg-laden aerosol generated from the evaporator stage was injected through an orifice into the non-thermal plasma reactor along with 60 sccm of an argon–silane mixture (1.36% SiH_4 in Ar) for in-flight coating. H_2 (30 sccm) was also added to the plasma to minimize the nucleation of Si particles and ensure that the silane precursor was used to coat the Mg NPs. The plasma reactor consists of a 2″ quartz tube and copper parallel plate electrodes, to which a radiofrequency (RF) signal was applied to sustain the discharge. The plasma reactor was maintained at a pressure of 1 Torr, and the RF power was 60 W at 13.56 MHz. The estimated residence time in the plasma reactor, based on flow velocity, was ≈185 ms. The coated particles were collected onto a stainless-steel mesh filter downstream of the plasma reactor. The NPs were extracted from the vacuum system after slowly leaking air to prevent ignition.

2.2. Preparation of Nanothermite Composites

Mg, Si, and coated Mg (Mg/Si–SiO_x) powders were added to the Bi_2O_3 oxidizer in hexanes followed by ultrasonication to achieve three homogeneous mixtures. The samples were dried for 24 h under ambient conditions to obtain the thermite powders. Different fuel samples (Mg, Si, and Mg/Si–SiO_x) with stoichiometric equivalents of Bi_2O_3 oxidizer (fuel:oxidizer equivalence ratio, $\phi = 1$) were mixed into nanothermite composites.

2.3. T-Jump/TOFMS and Ignition Characterization

Temperature-jump time-of-flight mass spectrometry (T-Jump/TOFMS) was performed to probe the reaction mechanisms in the different energetic composites at high heating rates.[25] The dispersed composites were coated on a Pt wire and resistively ignited using a rapid thermal pulse (≈3 ms). The pulse heated the wire rapidly to ≈1000–1200 °C, yielding a high heating rate of ≈10^5 °C s^{-1}. The gas-phase product species evolved from

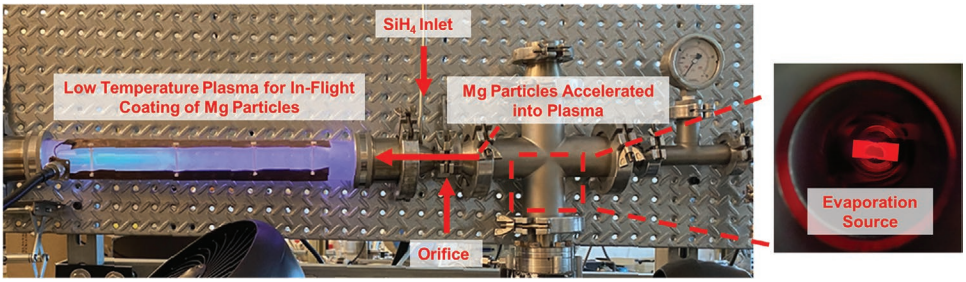

Figure 1. Photograph of the thermal evaporation system configured with a non-thermal plasma reactor in operation.

the thermally activated reactions in the samples were ionized using a 70 eV electron gun and accelerated toward a multichannel plate detector maintained at ≈1500 V. As a result, the mass spectra were obtained with a high temporal resolution (0.1 ms) and within timescales relevant to the rapid combustion reactions (≈1 ms). For ignition characterization, the thermite composites were coated on a Pt wire in an argon atmosphere followed by resistive pulse heating ignition, as described above. Simultaneously, a high-speed camera (Vision Research Phantom V12.1) was used to record the ignition event. The current across the Pt wire was measured using a Teledyne LeCroy CP030A current probe to obtain the wire temperature, which was determined from the current–voltage relationship using Callendar–Van Dusen equation.[26]

2.4. Materials Characterization

The morphology of the synthesized nanoparticles was characterized by scanning electron microscopy (SEM) with a ThermoFisher Scientific NNS450 microscope using a 20 kV accelerating voltage. Energy dispersive X-ray spectroscopy with an Oxford Instruments AztecSynergy Software and a 50 mm^2 X-Max50 SDD detector was utilized to obtain elemental analysis. A FEI Titan Themis 300 microscope was used to obtain high-angle annular dark-field (HAADF) images along with the elemental mapping of Mg, Si, and O content of the samples using the EDS detector. Transmission electron microscope (TEM) grids were prepared by ultrasonicating sample powder in isopropanol and drop-casting the particle solution onto lacey-carbon grids. X-ray diffraction (XRD) via a PANalytical Empyrean Series 2 was performed to investigate the crystallinity and composition of the samples. X-ray photoelectron spectroscopy (XPS) by a Kratos AXIS Ultra DLD was carried out to examine the surface composition and oxidation states of the atoms at the surface of the nanoparticle. Differential scanning calorimetry (DSC) was performed using a Netsch STA449 F3 Jupiter analyzer to monitor the oxidation of samples with a slow heating rate of 10 °C min^{-1}. In situ TEM using a JEOL JEM-ARM300F Grand ARM TEM instrument was utilized to analyze structural and morphological evolution while heating (10 °C min^{-1}) under vacuum.

3. Results and Discussion

3.1. Characterization of Synthesized Nanoparticles

SEM was used to analyze the morphology and size of the Mg NPs produced via thermal evaporation. **Figure 2**a–c shows

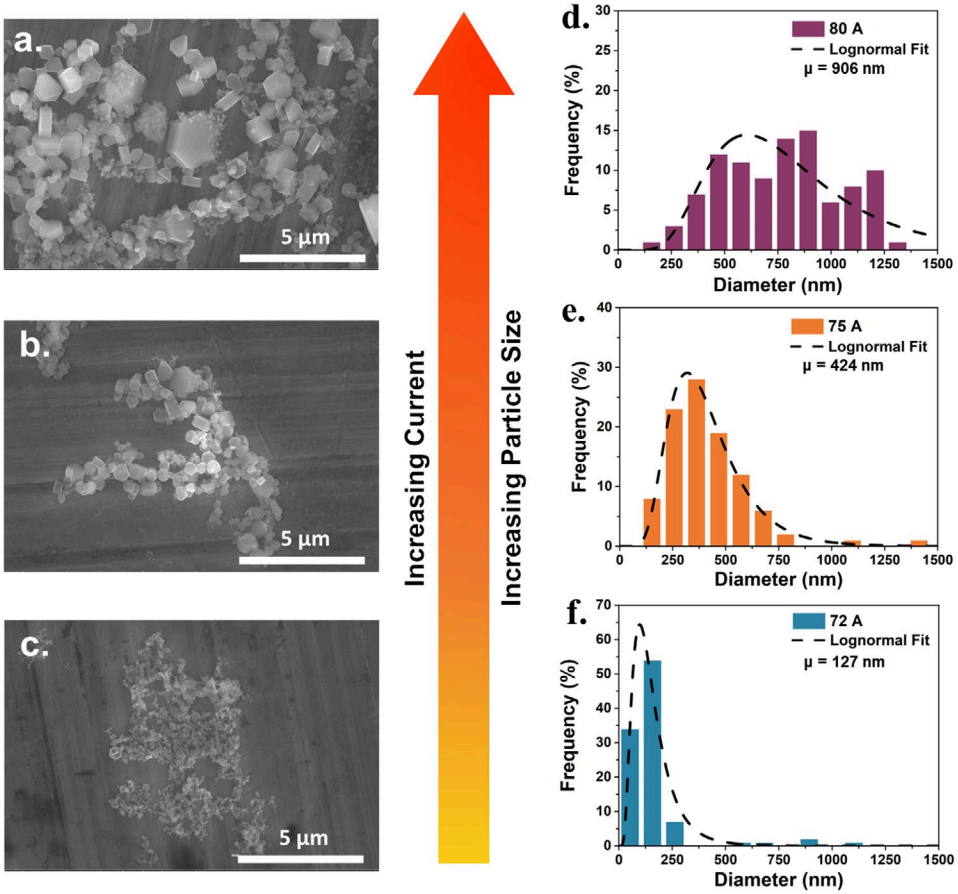

Figure 2. SEM images of Mg particles produced by thermal evaporation followed by gas-condensation using a) 80 A, b) 75 A, and c) 72 A of DC current with their correlated size distributions d–f).

the SEM images of Mg particles synthesized using various DC currents with their respective size distributions shown in Figure 2d–f. The crystals show hexagonal plate shapes, which is the thermodynamically favorable since the (0001) plane is close-packed and has the lowest free energy.[27] For completeness, we have performed XRD of these particles, confirming their hexagonal structure (Figure S2, Supporting Information). Note that the size of the particles increases as current supplied to the tungsten boat increases. The average nanoparticle size is 127, 424, and 906 nm, at currents of 72, 75, and 80 A, respectively. The size distributions are reasonably well fitted with lognormal size distributions. We observed a broadening of the size distribution with increasing current, with the geometric standard deviations (σ_g) being 1.5–1.6 for the three evaporation conditions. This is attributed to the increasing rate of Mg evaporation at higher current (more heating), causing larger vapor saturation ratios within the evaporation chamber. The critical cluster size and free energy barrier for homogeneous nucleation is lower at larger saturation ratios, leading to an increase in particle number density and to an increased rate of particle coagulation.[28] The size distributions were obtained by measuring the diameters of 100 hexagonal crystals synthesized at each current values using the SEM images in ImageJ software (version 1.53k). The estimated particle aspect ratio is roughly 0.35, and we did not observe any quantifiable dependence of aspect ratio over current density. Mg NPs and Mg/Si–SiO_x NPs were synthesized using 74 A of DC current, and the morphology of these NPs was analyzed by TEM (Figure S3a,b, Supporting Information). The average particle size for Mg NPs and Mg/Si–SiO_x NPs are 361 and 317 nm, respectively (Figure S3c,d, Supporting Information).

SEM and EDS were used to confirm the morphology and composition of Mg/Si–SiO_x particles (Figure S4, Supporting Information). The particles in the electron micrograph (Figure S4a, Supporting Information) show hexagonal morphology with apparent surface roughness, which may be attributed to smaller Si particles residing at the Mg particle surface. This was confirmed by the EDS elemental maps shown in Figure S4b–e (Supporting Information) that show Mg particles coated with Si, and with small Si particles on the Mg surface. Compositional analyses suggest that the Mg-to-Si atomic ratio is 3:1. Characterization and analysis of the plasma coating were performed by STEM with EDS elemental maps in **Figure 3**. A uniform oxide shell is confirmed on uncoated Mg particles (Figure 3a). Pores are observed around the edges of Mg crystals, which is indicative of the porous nature of the MgO layer when the bare Mg NPs are exposed to air. By comparison, STEM-EDS images of the Mg/Si–SiO_x particles (Figure 3b) suggest that the non-thermal plasma coating process is successful in applying a conformal Si shell around Mg particles. Based on STEM-EDS, the thickness of the Si layer on the Mg particles is ≈15 nm.

XPS characterization was performed to analyze the surface chemical configuration of Mg NPs with and without the silicon-based coating. The O 1*s* peak ≈531 eV is shown in **Figure 4**a. To better interpret the data, we have also performed XPS analysis on Mg NPs without surface coating (Mg control) and on

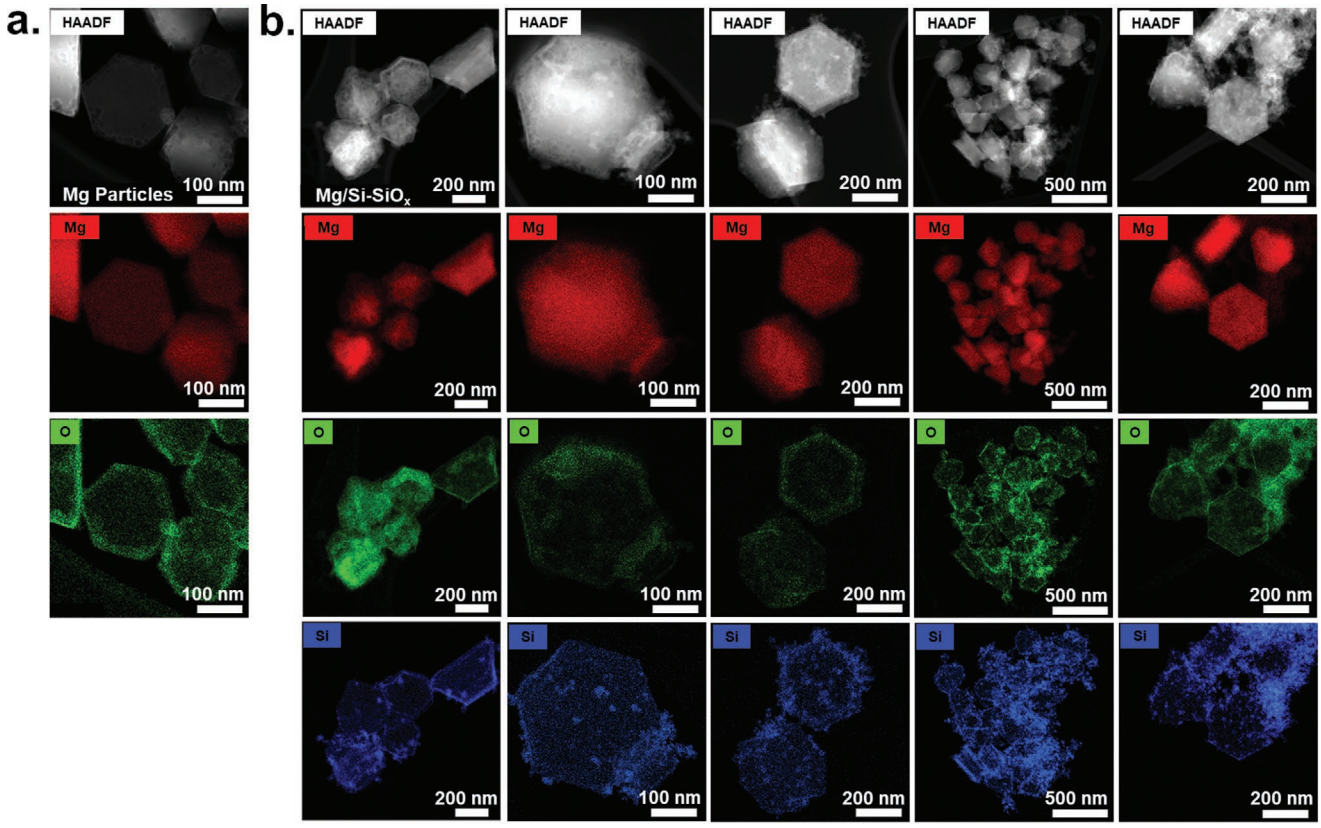

Figure 3. STEM-HAADF images and EDS elemental maps of a) uncoated Mg NPs and b) Mg/Si–SiO_x NPs.

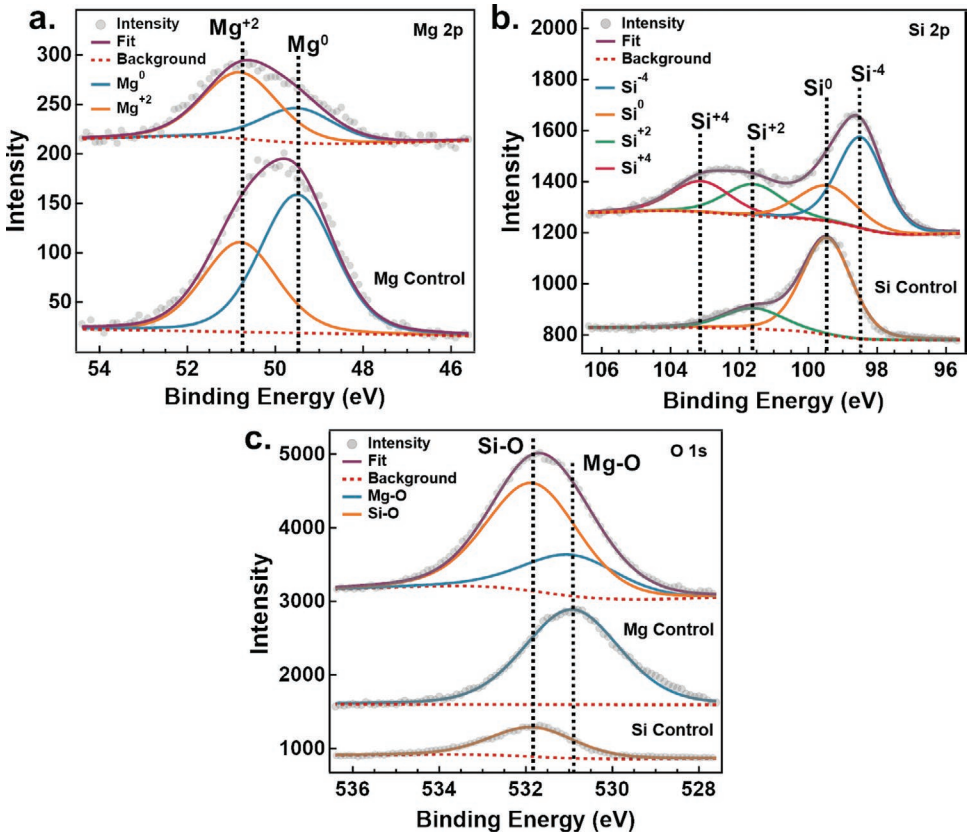

Figure 4. XPS of the Mg/Si–SiO_x particles, Mg control, and Si control showing the a) O 1s peaks, b) Si 2*p* peaks, and c) Mg 2*p* peaks.

Si nanoparticles produced using the same reactor, but without nucleating Mg NPs (Si control). For the Mg NPs with in-flight coating, we can distinguish contributions from both Si—O at ≈532 eV[29] and Mg—O at 531 eV,[30] although the dominant contribution is from Si—O suggesting that most of the oxygen is bound to silicon for the coated Mg NPs. The Si 2*p* peak ≈100 eV is shown in Figure 4b for both the coated Mg NPs and for the Si control. For the control, we can identify two peaks assigned to ground state Si at 99.5 eV and to SiO at 101.6 eV.[31] The Si 2*p* spectrum for the Mg/Si–SiO_x particles is more complex. We observe additional peaks, which we attribute to Mg_2Si at 98.4 eV and to SiO_2 at 103.1 eV.[31,32] This suggests that the silicon-based coating is oxidized, with contributions from both SiO and SiO_2 bonding. It also suggests that some of the silicon is bound directly to Mg, which is to be expected given the fact that the coating is applied before the particles are ever exposed to air. For completeness, we also show the Mg 2*p* peak ≈50 eV for the Mg control case and for the coated particles in Figure 4c. For the control case, we find two peaks corresponding to ground state Mg at 49.5 eV and MgO at 50.8 eV.[33] There is a slight blueshift for the Mg/Si–SiO_x particles, which in a counterintuitive manner suggests that the magnesium is more oxidized for the in-flight coated particles. Given the high degree of silicon oxidation, it is clear that oxygen can diffuse through the shell and still reach the magnesium core. We should point out that the Mg 2*p* signal is quite low for the case of the coated particles because the Mg is buried underneath the SiO_x layer. Because of this, the XPS analysis is more sensitive to the outermost portion of the Mg core, i.e., the one that is reached by oxygen. This explains the higher contribution from MgO bonding for the coated particles compared to the control sample (Mg NPs with native oxide). Overall, the combination of STEM-EDS and XPS confirms the successful coating of the Mg particles with a silicon-based shell. The shell is oxidized upon exposure to air. Direct bonding between Mg and Si is present at the interface between the Mg core of the silicon-based shell.

3.2. Reactive Properties

Ignition characterization was carried out by temperature-jump time-of-flight mass spectrometry (Tjump-TOFMS) and high-speed camera capture during combustion with an oxidizer in vacuum.[25a,34] A previous study on the ignition of Mg NPs with different oxidizers carried out by Ghildiyal et al. showed that the availability and release of Mg vapor directly impacted ignition and energetic performance.[5b] Oxidizers, such as Bi_2O_3 and copper oxide (CuO) decompose after the release of Mg vapor. As a result, using Bi_2O_3 as the oxidizer allows us to probe how surface modification affects the reaction rate-limiting step, i.e., the release of Mg vapor.[35] Different fuel samples (Mg and Mg/SiOx) prepared with the plasma reactor are incorporated with stoichiometric equivalents of Bi_2O_3 oxidizer (fuel:oxidizer equivalence ratio, $\phi = 1$) into nanothermite composites. The coated samples were also characterized against Mg and Si controls to investigate the effects of surface modification on ignition and

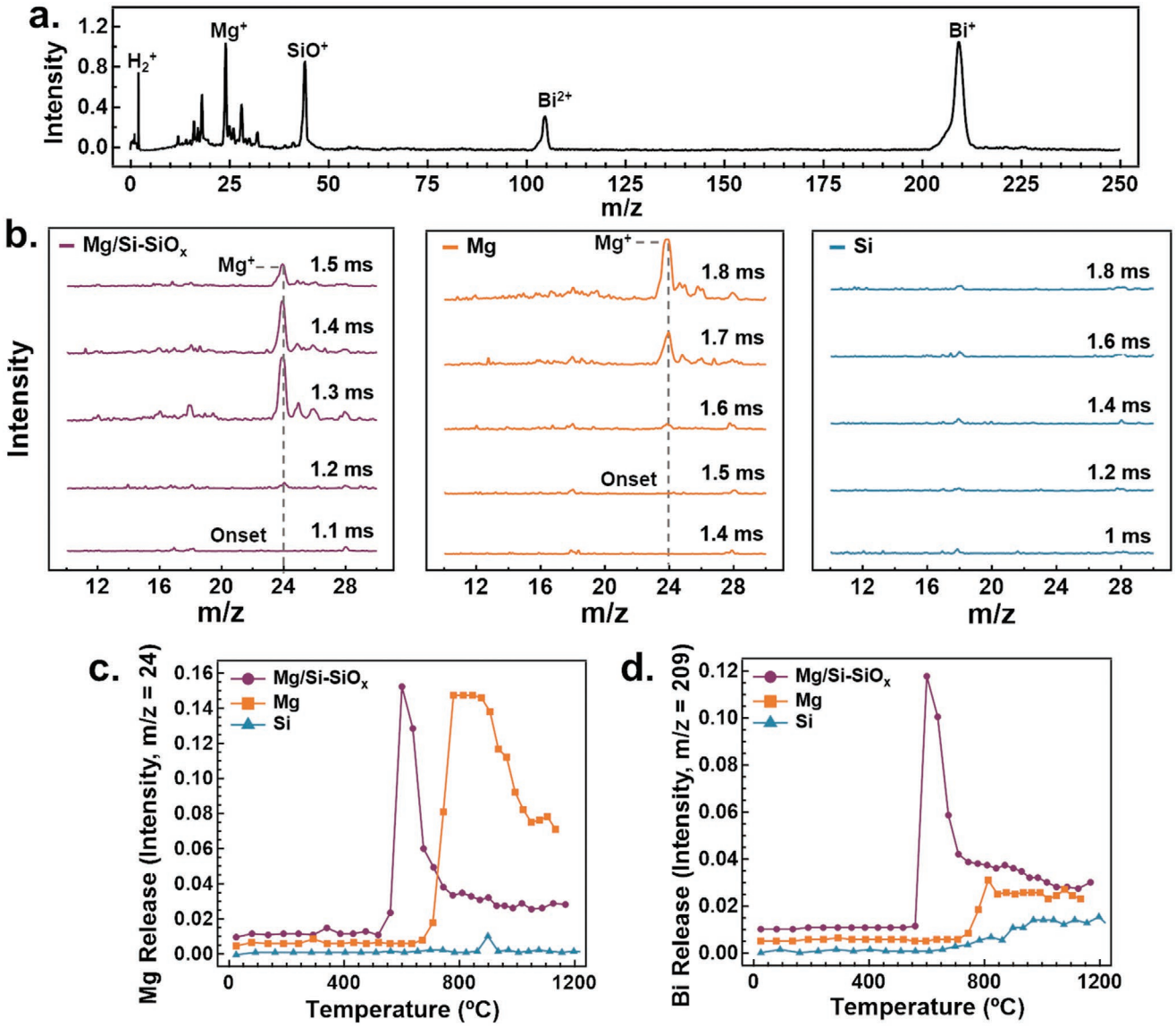

Figure 5. a) Tjump-TOFMS full spectrum data for the Mg/Si–SiO_x NPs. b) Timed spectra for Mg/Si–SiO_x NPs, Mg control, and Si control samples showing the evolution of Mg (m/z = 24) release. The c) Mg release profiles, and the d) Bi release profiles for Mg/Si–SiO_x NPs, Si control, and Mg control.

reaction mechanism. The Si control was synthesized under the same plasma reactor conditions used for the Mg/Si–SiO_x NPs, but without supplying current to the thermal evaporator, hence eliminating Mg particles in the process. A constant equivalence ratio ($\phi = 1$) is maintained for all the samples.

Figure 5a is a representative full spectrum of the T-Jump/TOFMS, showing the combustion product species evolved during ignition of the coated Mg sample. The Mg release over time for Mg/Si–SiO_x NPs, Mg control, and Si control are shown in Figure 5b. There is no Mg release from the Si control since there is no Mg present. The Mg release onset for the coated Mg occurs ≈0.4 ms earlier than the Mg control. Figure 5c,d provides the temporal release of Mg and bismuth (Bi) when samples are rapidly heated until combustion, respectively. Both Mg and Bi were released earlier and at lower temperatures for the coated samples compared to uncoated Mg and Si. Timestamped images of ignited Si, Mg, and Mg/Si–SiO_x NPs are shown in **Figure 6**a–c, respectively. The ignition temperature, as obtained from high-speed imaging, showed that optical emission occurs at a significantly lower temperature for Mg/Si–SiO_x NPs (≈520 °C) compared to non-coated Mg (≈740 °C). The ignition of the Mg/Si–SiO_x NPs completes in ≈0.1 ms as opposed to ≈0.3 ms for the Mg control, suggesting reduced ignition thresholds for coated particles. The Si control does not show any significant combustion, ruling out the contribution from Si itself to the overall energetic reaction. Additionally, the decomposition of Bi_2O_3 results in the release of gaseous Bi at temperatures above 870 °C.[35] The early onset of both Bi and Mg release for the Mg/Si–SiO_x NPs is consistent with a localized exothermic reaction, which accelerates combustion. Overall, the

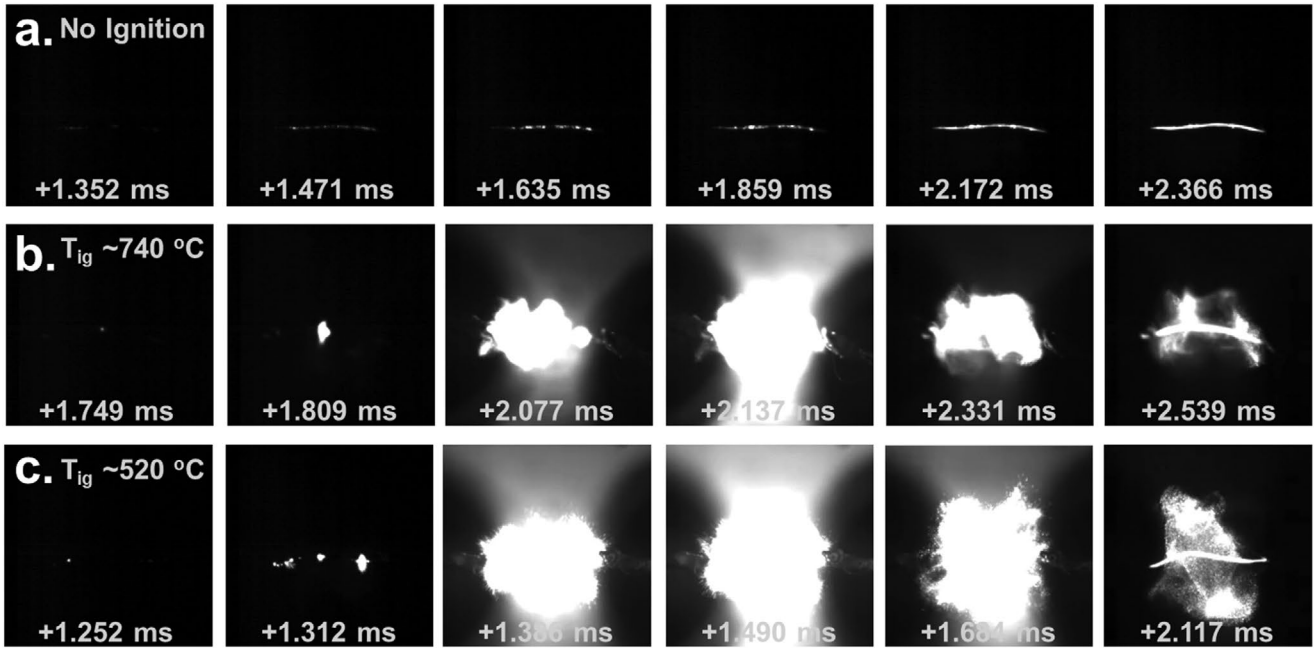

Figure 6. High-speed camera imaging during ignition for a) Si with Bi_2O_3, b) Mg with Bi_2O_3, and c) Mg/Si–SiO_x with Bi_2O_3.

Tjump-TOFMS data along with the high-speed camera capture conclusively shows that the non-thermal plasma surface modification has a direct and beneficial effect on the energetic performance of the fuel particles. The observed reduced ignition onset is not due to size effects because the difference in average size between the Mg and the Mg/Si–SiO_x NPs is minimal, as shown in Figure S3 (Supporting Information). As shown in previous work by Ghildiyal et al., the difference in ignition temperature for 500 and 40 nm Mg particles is ≈140 °C,[5b] i.e., a significantly smaller reduction than in the case of our coated NPs.

The ignition mechanisms were further investigated by DSC in an ultra-high purity argon environment, as shown in **Figure 7**a. The products were analyzed via XRD, see Figure 7b. The as produced particles show the expected Mg peaks according to the hexagonal close-packed crystal structure with the major peak at 36.8° corresponding to the (10–11) plane, and a small Mg_2Si peak at ≈40° according to the (220) plane. We did not observe any peak from silicon, suggesting that the shell is amorphous. DSC shows a first exotherm upon heating to ≈400 °C. The corresponding XRD spectrum indicates that the Mg peaks are reduced while the Mg_2Si peaks increase in intensity. This correlates with a condensed-phase alloying reaction occurring at the interface between the Mg core and the Si–SiO_x shell. Further heating to 750 °C leads to a second exotherm, with the corresponding XRD showing peaks from Si with the major peak at 28.2° according to the (111) plane, and from MgO with the prominent peak at 42.4° according to the (200) plane. Therefore, we interpret this second exothermic reaction as the magnesiothermic reduction of the oxidized silicon shell by the Mg core.

The combination of DSC and XRD data suggests that there is a two-step ignition process for Mg/Si–SiO_x samples, as indicated by Equations 1 and 2.[36]

$$2\mathrm{Mg(s)} + \mathrm{Si(s)} \rightarrow \mathrm{Mg_2Si(s)} \qquad \Delta H_f^{\circ} = -39\ \mathrm{kJ\ mol^{-1}\ of\ Mg} \tag{1}$$

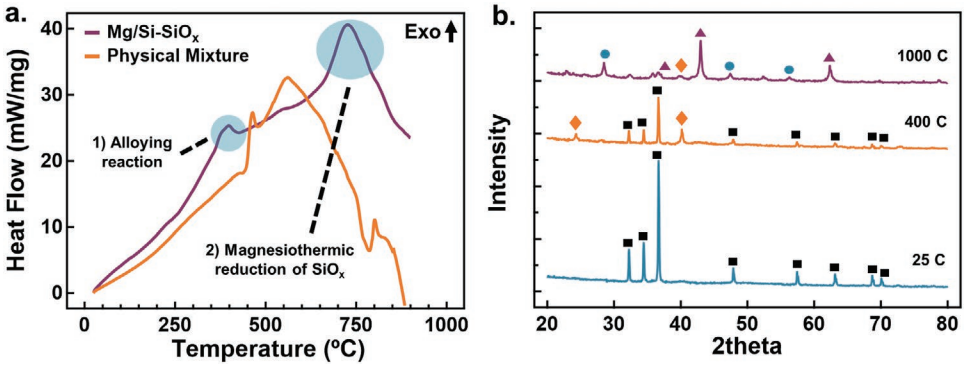

Figure 7. a) DSC profile for Mg/Si–SiO_x particles performed in ultra-high purity Ar. b) XRD of the Mg/Si–SiO_x samples heated to 400 and 1000 °C and analyzed against an unheated sample. The blue circles, black squares, purple triangles, and orange diamonds indicate Si, Mg, MgO, and Mg_2Si, respectively.

$$2Mg(s) + SiO_2(s) \rightarrow 2MgO(s) + Si(s) \quad \Delta H^{\circ}_{rxn} = -146\ kJ\ mol^{-1}Mg \quad (2)$$

The calculated adiabatic temperatures for the reduction of SiO_2 by Mg can reach ≈2300 °C,[37] and Mg_2Si formation can reach ≈1000 °C,[38] supporting the conclusion that the heat generated by the reaction between Mg core and the Si–SiO_x shell is more than sufficient to trigger Mg release and initiate combustion when mixed with Bi_2O_3. The onset temperature of magnesiothermic reduction has been reported over a wide range of values, where onset temperatures are expected from ≈460 °C to above ≈650 °C, and the reaction heightens when the Mg vapor pressure is sufficiently high to diffuse into SiO_2.[37a,39] Below 650 °C, a solid-state reaction occurs that includes the formation of Mg_2Si.[39a] We observe the formation of Mg_2Si for Mg/Si–SiO_x NPs at a lower temperature of ≈400 °C, which suggests the close proximity of Si at the interface allows a lower reaction onset temperature.

Additionally, we have performed DSC on a physical mixture of Si–SiO_x NPs and Mg NPs to investigate whether the close proximity between the Mg fuel and the Si–SiO_x shell plays a role in lowering the ignition temperature. Two exothermic peaks are apparent in the DSC curve; however, they occur at higher temperatures compared to the in-flight coated samples. We conclude that the reduced reaction onset temperature for Mg/Si–SiO_x NPs (≈400 °C) observed in DSC can be attributed to the direct contact between the Mg core and the Si–SiO_x layer, allowing shorter diffusion lengths, faster kinetics, and lower onset of the exothermic reaction. The faster Mg and Bi release for Mg/Si–SiO_x NPs observed in the T-jump/TOFMS, for the case of combustion with Bi_2O_3 as solid-state oxidizer (see Figure 5), can therefore be attributed to interfacial reactions enabling the release of Mg vapor at a lower temperature, resulting in earlier reaction onset between Bi_2O_3 and Mg.

Finally, we have performed in situ TEM analysis to monitor changes in particle morphology during heating in vacuum under slow heating (10 °C min^{-1}). The in situ TEM videos of Mg NPs and Mg/Si–SiO_x NPs are provided in Videos S1 and S2 (Supporting Information), respectively. **Figure 8**a,b depicts snapshots at different temperatures of Mg/Si–SiO_x NPs and Mg NPs, respectively. For both cases, we observe outward-diffusion of Mg resulting in hollowing of the particles, consistent with recent findings from Ghildiyal et al.[5b] The onset of core vaporization of Mg for the coated particles occurs at ≈240 °C compared to ≈340 °C for uncoated Mg particles. This is consistent with the data shown in Figure 7. Early access to the Mg fuel explains the decreased ignition and release temperatures

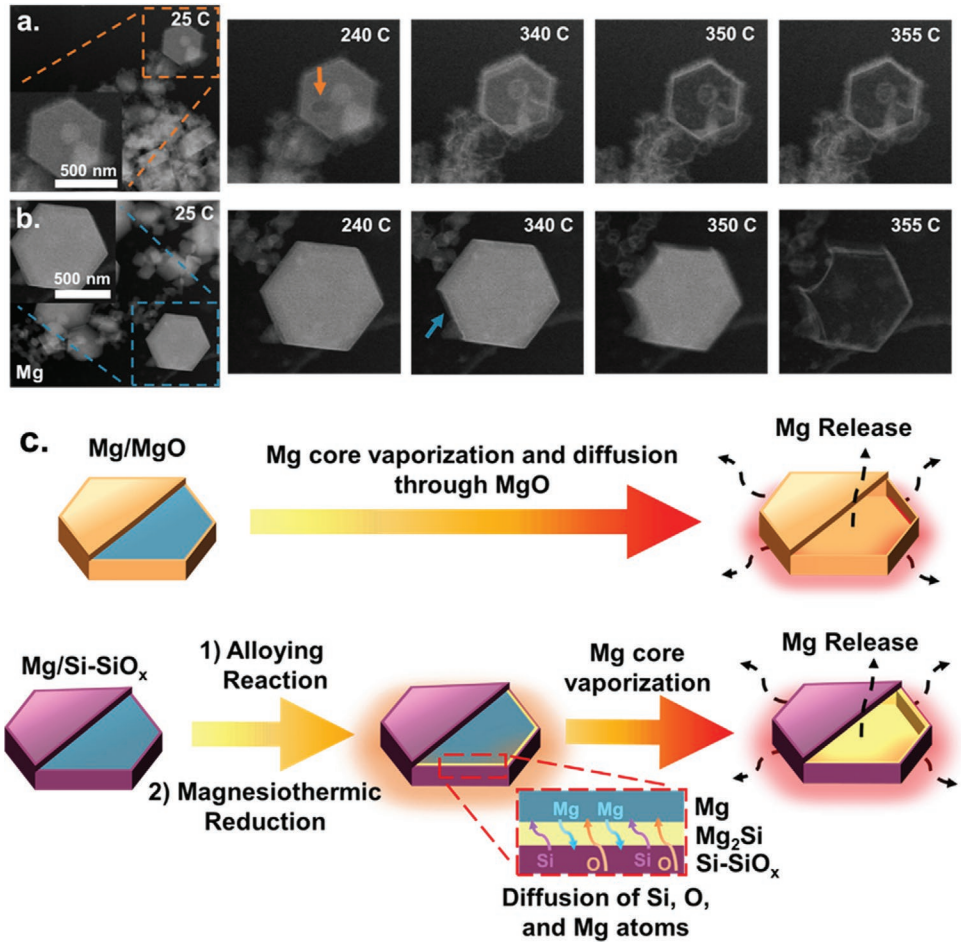

Figure 8. In situ TEM micrographs of a) Mg/Si–SiO_x NPs and b) Mg NPs under a heating rate of 10 °C min^{-1}. c) Schematic showing the ignition pathways for Mg and Mg/Si–SiO_x particles.

for the reaction of Mg/Si–SiO_x NPs with Bi_2O_3 (Figure 5). We should point out that while the hollowing of the Mg/Si–SiO_x NPs starts considerably earlier compared to the Mg NPs, it also finishes at ≈350 °C, corresponding to a ΔT of 110 °C. Hollowing of the Mg NPs finishes at ≈355 °C, which is a ΔT of 15 °C. The localized release of energy at the Mg core/Si–SiO_x shell interface leads to Mg vaporization at a lower temperature, although outward-diffusion of Mg seems slower for the case of the coated sample. This is likely due to the presence of a thicker shell for the case of the in-flight coated material. We should point out that the evaporation of the Mg core occurs at a much lower temperature (≈240 °C) than the oxidation onset observed by DSC (≈400 °C). The sample size for in situ TEM studies is considerably smaller (a handful of particles) compared to DSC (several mg of powder characterized at once). A study by Mahadevan et al. shows that decreasing sample size influences the measured reaction kinetics due to heat and mass transport effects.[40] In situ TEM measurements can increase the particle temperature up to 200 K, which could be another reason for the earlier Mg evaporation temperature than the Mg release and oxidation onset temperatures from Tjump/TOFMS and DSC, respectively.[41] A schematic summarizing the ignition mechanism of Mg NPs versus Mg/Si–SiO_x NPs is outlined in Figure 8c. For the case of Mg with a native oxide shell, the metal vaporizes within the core and diffuses outward through a porous oxide shell to react with an oxidizer. For the coated sample, the Mg core is surrounded by a Si–SiO_x layer. Upon heating, an intermetallic reaction takes place first followed by the magnesiothermic reduction of the oxidized shell. These reactions are exothermic with high predicted adiabatic temperatures, triggering the early release of Mg vapor and further reaction with the surrounding oxidizer.

4. Conclusion

In conclusion, we have investigated the surface modification of magnesium NPs and its effect on the material combustion properties. We have leveraged the capabilities of low-temperature plasmas to apply a conformal silicon-based coating onto the surface of magnesium NPs. This is done in-flight, immediately after the nucleation and growth of the magnesium particles and before exposure to air. We demonstrate that the ignition temperature and the reaction rate of Mg particles with Bi_2O_3 can be considerably altered by the presence of a silicon-based shell. Differential scanning calorimetry, detailed structural analysis by XRD and in situ TEM during heating in an inert environment confirm both the formation of magnesium silicide and the occurrence of a magnesiothermic reaction between the magnesium core and the silicon oxide shell. T-jump measurements confirm that the coated particles show a significant reduction in ignition temperature (>200 °C) during combustion with Bi_2O_3, consistent with an earlier onset of release of Mg vapor from the fuel particles when these are coated with the silicon-based shell. This work demonstrates that improvements in the combustion of Mg particles, which have received less attention than the more widely investigated Al, are easily within reach with the appropriate surface modification approach. We stress that further improvements are likely within reach by further optimization of coating thickness and magnesium core size.

Supporting Information

Supporting Information is available from the Wiley Online Library or from the author.

Acknowledgements

B.W. and P.G. contributed equally to this work. This work was supported by the DTRA – Materials Science in Extreme Environments University Research Alliance (MSEE – URA). Electron microscopy was performed on a FEI Titan Themis 300 in the Central Facility for Advanced Microscopy and Microanalysis at UC Riverside. The authors acknowledge the use of facilities and instrumentation (JEOL JEM-ARM300F Grand ARM TEM) at the UC Irvine Materials Research Institute (IMRI), which is supported in part by the National Science Foundation through the UC Irvine Materials Research Science and Engineering Center (DMR-2011967).

Conflict of Interest

The authors declare no conflict of interest.

Data Availability Statement

The data that support the findings of this study are available from the corresponding author upon reasonable request.

Keywords

coating, combustion, ignition, magnesium, non-thermal plasma, silicon

Received: November 3, 2022
Revised: January 25, 2023
Published online:

[1] R. A. Yetter, *Proc. Combust. Inst.* **2021**, *38*, 57.
[2] a) T. Hawa, M. R. Zachariah, *J. Aerosol Sci.* **2007**, *38*, 793; b) R. A. Yetter, G. A. Risha, S. F. Son, *Proc. Combust. Inst.* **2009**, *32*, 1819; c) R. Thiruvengadathan, in *Nano-Energetic Materials* (Eds: S. Bhattacharya, A. K. Agarwal, T. Rajagopalan, V. K. Patel), Springer, Singapore **2019**, p. 9.
[3] a) D. Sundaram, V. Yang, R. A. Yetter, *Prog. Energy Combust. Sci.* **2017**, *61*, 293; b) B. Van Devener, J. P. L. Perez, J. Jankovich, S. L. Anderson, *Energy Fuels* **2009**, *23*, 6111.
[4] a) R. Lomba, S. Bernard, P. Gillard, C. Mounaïm-Rousselle, F. Halter, C. Chauveau, T. Tahtouh, O. Guézet, *Combust. Sci. Technol.* **2016**, *188*, 1857; b) M. Akiyama, K. Nishii, Y. Mannami, M. Murohara, H. Koizumi, K. Komurasaki, *Trans. Jpn. Soc. Aeronaut. Space Sci.* **2021**, *64*, 223; c) C. K. Law, F. A. Williams, *Combust. Flame* **1974**, *22*, 383; d) W. Zeng, C. O. Nyapete, A. Benziger, P. A. Jelliss, S. W. Buckner, *Curr. Appl. Polym. Sci.* **2019**, *3*, 3.
[5] a) I. Shancita, N. G. Vaz, G. D. Fernandes, A. J. A. Aquino, D. Tunega, M. L. Pantoya, *Combust. Flame* **2021**, *226*, 419; b) P. Ghildiyal, P. Biswas, S. Herrera, F. Xu, Z. Alibay, Y. Wang, H. Wang, R. Abbaschian, M. R. Zachariah, *ACS Appl. Mater. Interfaces* **2022**, *14*, 17164.

[6] a) A. Zolotko, A. Matsko, D. Polishchuk, S. Buinovskii, L. Gaponenko, *Combust., Explos. Shock Waves* **1980**, *16*, 20; b) A. Breiter, V. Mal'tsev, E. Popov, *Combust., Explos. Shock Waves* **1990**, *26*, 86; c) L. T. DeLuca, F. Maggi, S. Dossi, M. Fassina, C. Paravan, A. Sossi, In *Chemical Rocket Propulsion*, Springer, Berlin, Germany **2017**, p. 191.
[7] a) K. K. Miller, I. Shancita, S. K. Bhattacharia, M. L. Pantoya, *Mater. Des.* **2021**, *210*, 110119; b) D. W. Kim, K. T. Kim, G. H. Kwon, K. Song, I. Son, *Sci. Rep.* **2019**, *9*, 1033; c) R. J. Jouet, A. D. Warren, D. M. Rosenberg, V. J. Bellitto, K. Park, M. R. Zachariah, *Chem. Mater.* **2005**, *17*, 2987; d) D. A. Kaplowitz, G. Jian, K. Gaskell, A. Ponce, P. Shang, M. R. Zachariah, *Part. Part. Syst. Charact.* **2013**, *30*, 881.
[8] F.-Y. Guan, H. Ren, W.-J. Zhao, X.-Z. Wu, Q.-J. Jiao, *Def. Technol.* **2021**, *18*, 1852.
[9] Y. Jiang, Y. Wang, J. Baek, H. Wang, J. L. Gottfried, C.-C. Wu, X. Shi, M. R. Zachariah, X. Zheng, *Combust. Flame* **2022**, *242*, 112170.
[10] T. J. Foley, C. E. Johnson, K. T. Higa, *Chem. Mater.* **2005**, *17*, 4086.
[11] R. Ali, F. Ali, A. Zahoor, R. N. Shahid, N. U. H. Tariq, G. Ali, S. Ullah, A. Shah, H. B. Awais, *J. Energ. Mater.* **2022**, *40*, 243.
[12] S.-H. Zhang, *Trans. Nonferrous Met. Soc. China* **2006**, *16*, S285.
[13] D. L. Hastings, M. Schoenitz, K. M. Ryan, E. L. Dreizin, J. W. Krumpfer, *Propellants, Explos., Pyrotech.* **2020**, *45*, 621.
[14] a) A. Woodard, L. Xu, A. A. Barragan, G. Nava, B. M. Wong, L. Mangolini, *Plasma Processes Polym.* **2018**, *15*, 1700104; b) J. Schwan, B. Wagner, M. Kim, L. Mangolini, *J. Phys. D: Appl. Phys.* **2021**, *55*, 094002; c) A. A. Barragan, S. Hanukovich, K. Bozhilov, S. S. R. K. C. Yamijala, B. M. Wong, P. Christopher, L. Mangolini, *J. Phys. Chem. C* **2019**, *123*, 21796.
[15] a) V. Cech, M. Branecky, *Plasma Processes Polym.* **2022**, *19*, 2100192; b) E. Thimsen, M. Johnson, X. Zhang, A. J. Wagner, K. A. Mkhoyan, U. R. Kortshagen, E. S. Aydil, *Nat. Commun.* **2014**, *5*, 5822.
[16] a) E. Liston, L. Martinu, M. Wertheimer, *J. Adhes. Sci. Technol.* **1993**, *7*, 1091; b) M. Gu, J. E. Kilduff, G. Belfort, *Biomaterials* **2012**, *33*, 1261.
[17] a) W. He, Z. Guo, Y. Pu, L. Yan, W. Si, *Appl. Phys. Lett.* **2004**, *85*, 896; b) R. J. Anthony, D. J. Rowe, M. Stein, J. Yang, U. Kortshagen, *Adv. Funct. Mater.* **2011**, *21*, 4042.
[18] a) U. Kortshagen, U. Bhandarkar, *Phys. Rev. E* **1999**, *60*, 887; b) T. Matsoukas, M. Russell, *J. Appl. Phys.* **1995**, *77*, 4285; c) D. Graves, J. Daugherty, M. Kilgore, R. Porteous, *Plasma Sources Sci. Technol.* **1994**, *3*, 433.
[19] a) U. R. Kortshagen, R. M. Sankaran, R. N. Pereira, S. L. Girshick, J. J. Wu, E. S. Aydil, *Chem. Rev.* **2016**, *116*, 11061; b) F. Xu, G. Nava, P. Biswas, I. Dulalia, H. Wang, Z. Alibay, M. Gale, D. J. Kline, B. Wagner, L. Mangolini, M. R. Zachariah, *Chem. Eng. J.* **2022**, *430*, 133140.
[20] O. Yasar-Inceoglu, L. Zhong, L. Mangolini, *J. Phys. D: Appl. Phys.* **2015**, *48*, 314009.
[21] R. P. Chaukulkar, K. D. Peuter, P. Stradins, S. Pylypenko, J. P. Bell, Y. Yang, S. Agarwal, *ACS Appl. Mater. Interfaces* **2014**, *6*, 19026.
[22] K. I. Hunter, J. T. Held, K. A. Mkhoyan, U. R. Kortshagen, *ACS Appl. Mater. Interfaces* **2017**, *9*, 8263.
[23] a) C. Berrospe Rodriguez, A. Alvarez Barragan, G. Nava, S. Exarhos, L. Mangolini, *ACS Appl. Nano Mater.* **2020**, *3*, 4504; b) D. Coleman, L. Mangolini, *ACS Omega* **2019**, *4*, 10089; c) S. Exarhos, A. Alvarez-Barragan, E. Aytan, A. A. Balandin, L. Mangolini, *ACS Energy Lett.* **2018**, *3*, 2349.
[24] N. Rajput, *Int. J. Adv. Eng. Technol.* **2015**, *7*, 1806.
[25] a) L. Zhou, N. Piekiel, S. Chowdhury, M. R. Zachariah, *Rapid Commun. Mass Spectrom.* **2009**, *23*, 194; b) P. Ghildiyal, X. Ke, P. Biswas, G. Nava, J. Schwan, F. Xu, D. J. Kline, H. Wang, L. Mangolini, M. R. Zachariah, *ACS Appl. Mater. Interfaces* **2021**, *13*, 458.
[26] a) P. Biswas, F. Xu, P. Ghildiyal, M. R. Zachariah, *ACS Appl. Mater. Interfaces* **2022**, *14*, 26782; b) J. B. DeLisio, X. Hu, T. Wu, G. C. Egan, G. Young, M. R. Zachariah, *J. Phys. Chem. B* **2016**, *120*, 5534.
[27] E. Ringe, *J. Phys. Chem. C* **2020**, *124*, 15665.
[28] M. Raffi, A. K. Rumaiz, M. M. Hasan, S. I. Shah, *J. Mater. Res.* **2007**, *22*, 3378.
[29] Y. N. Sun, A. Feldman, E. N. Farabaugh, *Thin Solid Films* **1988**, *157*, 351.
[30] P. J. Burke, Z. Bayindir, G. J. Kipouros, *Appl. Spectrosc.* **2012**, *66*, 510.
[31] I. Mishra, S. Majumder, S. R. Joshi, U. Subudhi, S. Varma, *Chem. Phys.* **2022**, *562*, 111665.
[32] a) Y. Tsuboi, S. Ura, K. Takahiro, T. Henmi, A. Okada, T. Wakasugi, K. Kadono, *J. Asian Ceram. Soc.* **2017**, *5*, 341; b) J. Stuchlik, T. Ha Stuchlikova, A. Artemenko, Z. Remes, *JJAP Conference Proceedings* **2015**, *3*, 011301.
[33] F. Khairallah, A. Glisenti, *Surf. Sci. Spectra* **2006**, *13*, 58.
[34] M. C. Rehwoldt, Y. Wang, F. Xu, P. Ghildiyal, M. R. Zachariah, *ACS Appl. Mater. Interfaces* **2022**, *14*, 8938.
[35] X. Wang, T. Wu, H. Wang, J. B. DeLisio, Y. Yang, M. R. Zachariah, *Combust. Flame* **2018**, *197*, 127.
[36] a) I.-H. Jung, D.-H. Kang, W.-J. Park, N. J. Kim, S. Ahn, *Calphad* **2007**, *31*, 192; b) S. Cordova, E. Shafirovich, *Mater. Chem. Phys.* **2020**, *254*, 123288.
[37] a) B. Zhang, F. Wang, J. Chen, B. Li, K. Liu, Q. Han, *Silicon* **2022**, *14*, 8409; b) M. K. Zakaryan, S. V. Aydinyan, S. L. Kharatyan, *Silicon* **2017**, *9*, 841.
[38] a) M. Faraji, M. Adeli, M. Soltanieh, *Ceram. Int.* **2021**, *47*, 2822; b) X. Su, F. Fu, Y. Yan, G. Zheng, T. Liang, Q. Zhang, X. Cheng, D. Yang, H. Chi, X. Tang, Q. Zhang, C. Uher, *Nat. Commun.* **2014**, *5*, 4908.
[39] a) A. Darghouth, S. Aouida, B. Bessais, *Silicon* **2021**, *13*, 667; b) S. Haouli, S. Boudebane, I. J. Slipper, S. Lemboub, P. Gębara, S. Mezrag, *Phosphorus, Sulfur Silicon Relat. Elem.* **2018**, *193*, 280; c) K. Matsubara, H. Shiomi, T. Shiono, A. Okada, T. Wakasugi, K. Kadono, *Int. J. Ceram. Eng. Sci.* **2020**, *2*, 310.
[40] R. Mahadevan, D. Lee, H. Sakurai, M. R. Zachariah, *J. Phys. Chem. A* **2002**, *106*, 11083.
[41] T. Yokota, M. Murayama, J. M. Howe, *Phys. Rev. Lett.* **2003**, *91*, 265504.